11

Evaluation of the Respiratory Motion Effect in Small Animal PET Images with GATE Monte Carlo Simulations

Susana Branco[1], Pedro Almeida[1] and Sébastien Jan[2]
[1]*Instituto de Biofísica e Engenharia Biomédica Faculdade de Ciências da Universidade de Lisboa*
[2]*Service Hospitalier Frédéric Joliot Commissariat à l'Énergie Atomique*
[1]*Portugal*
[2]*France*

1. Introduction

The rapid growth in genetics and molecular biology combined with the development of techniques for genetically engineering small animals has led to increased interest in *in vivo* small animal imaging (Cherry & Gambhir, 2001; Riemann et al., 2008; Rowland & R., 2008). Small animal imaging has been applied frequently to the imaging of small animals (mice and rats), which are ubiquitous in modeling human diseases and testing treatments. The use of PET in small animals allows the use of subjects as their own control, reducing the interanimal variability. This allows performing longitudinal studies on the same animal and improves the accuracy of biological models (Cherry, 2004). However, small animal PET still suffers from several limitations. The amounts of radiotracers needed, limited scanner sensitivity, image resolution and image quantification issues, all could clearly benefit from additional research (Chatziioannou, 2002; Tai & Laforest, 2005).

Because nuclear medicine imaging deals with radioactive decay, the emission of radiation energy through photons and particles alongside with the detection of these quanta and particles in different materials make Monte Carlo method an important simulation tool in both nuclear medicine research and clinical practice. In order to optimize the quantitative use of PET in clinical practice, data- and image-processing methods are also a field of intense interest and development. The evaluation of such methods often relies on the use of simulated data and images since these offer control of the ground truth. Monte Carlo simulations are widely used for PET simulation since they take into account all the random processes involved in PET imaging, from the emission of the positron to the detection of the photons by the detectors. Simulation techniques have become an importance and indispensable complement to a wide range of problems that could not be addressed by experimental or analytical approaches (Rogers, 2006).

Monte Carlo methods are numerical calculation methods based on random variable sampling. This approach has been used to solve mathematical problems since 1770 and has been named "Monte Carlo" by Von Neumann because of the similarity of statistical simulations to games of chance, represented by the most well known center for gambling:

the Monte Carlo district in the Monaco principality. The general idea of Monte Carlo analysis is to create a model, which is as similar as possible to the real physical system of interest, and to create interactions within that system based on known probabilities of occurrence, with random sampling of the Probability Density Functions (PDFs). As the number of individual events (called histories) increase, the quality of the reported average behavior of the system improves, meaning that the statistical uncertainty decreases. Virtually, any complex system can in principle be modeled: if the distribution of events that occur in a system is know from experience, a PDF can be generated and sampled randomly to simulate the real system. A detailed description of the general principles and applications of the Monte Carlo method can be found elsewhere: (Andreo, 1991; Zaidi, 1999; Ljungberg, 1998, 2004; Zaidi & Sgouros, 2002; Zaidi, 2006).

The simulation of PET imaging using Monte Carlo allows the optimization of system design for new scanners, the study of factors affecting image quality, the validation of correction methodologies for effects such as scatter, attenuation and partial volume, for improved image quantification, as well as the development and testing of new image reconstruction algorithms. Another major advantage of simulations in nuclear medicine imaging is that they allow studying parameters that are not measurable in practice. The fraction of photons that are scattered in a phantom and their contribution to the image are examples of such parameters, and they can only be measured indirectly for a very limited number of geometries. In addition, in a computer model it is possible to turn off certain effects, such as photon attenuation and scattering in the phantom, which means that ideal images, which include camera-specific parameters, can be created and used as reference images. In combination with patient-like phantoms, the Monte Carlo method can be used to produce simulated images very close to those acquired from real measurements. In this context, Monte Carlo simulations are becoming an essential tool for assisting this research and some specific Monte Carlo simulation packages have been evaluated for nuclear medicine applications (Andreo & Ljungberg, 1998; Buvat & Castiglioni, 2002; Buvat et al., 2005; Buvat & Lazaro, 2006). Recently, the Geant4 Application for Tomographic Emission (GATE) platform has been developed (Jan et al., 2004a; GATE, 2010) and validated for the simulation of the microPET® FOCUS 220 system (Jan et al., 2005).

An important aspect of simulation is the possibility of having a realistic model (phantom) of the subject's anatomy and physiological functions from which imaging data can be generated using accurate models of the imaging process (Ljungberg, 2004; Zaidi, 2006; Zubal, 1998; Poston et al., 2002; Peter et al., 2000). Conceptually, the purpose of a physical or computerized phantom is to represent an organ or body region of interest, to allow modeling the biodistribution of a particular radiotracer and the chemical composition of the scattering medium, which absorbs and scatters the emitted radiation in a manner similar to biological tissues. In other terms, a phantom is a mathematical model designed to represent an organ or tissue of the body, an organ system, or the whole-body.

The widespread interest in molecular imaging spurred the development of more realistic 3D to 5D computational models based on the actual anatomy and physiology of individual humans and small animals. The advantage in using such phantoms in simulation studies is that the exact anatomy and physiological functions are known, thus providing a gold standard or truth in order to evaluate and improve imaging devices, data acquisition techniques, and imaging processing and reconstruction methods. Moreover, computer phantoms can be altered in order to model different anatomies and pathological situations. A review of the fundamental and technical challenges of designing computational models of the human anatomy can be found in (Zaidi & Xu, 2007; Zaidi & Tsui, 2009). These reviews summarize the latest efforts and future directions in the development of computational anthropomorphic models for application in radiological sciences.

Based on state-of-the-art computer graphics techniques, the 4D Mouse Whole Body (MOBY) phantoms provide a realistic model of the mouse anatomy and physiology for imaging studies (Segars et al., 2004). The phantom, when combined with accurate models for the imaging process, is capable of providing realistic imaging data from subjects with various anatomies and motions (cardiac and respiratory) in health and disease. With this ability, the phantom has enormous potential to help studying the effects of anatomical, physiological, physical, and instrumentation factors on small animal imaging and to research new instrumentation, image acquisition strategies, image processing and reconstruction methods as well as image visualization and interpretation techniques.

It is known that the localization and detection of thoracic and abdominal lesions in PET imaging is often perturbed due to the displacement of the organs during normal breathing. The respiratory motion compromise image quality and quantification in PET, and affect clinical diagnosis. Motion can actually introduce large biases, for instance tracer uptake underestimation greater than 50% in lung lesion. Moreover, respiratory motion can induce resolution degradation (blurring effect) for PET imaging. Contrast loss of small lesions in PET images due to the above motion blurring effect can adversely affect the lesion detection sensitivity for PET imaging of lung or liver cancers. The degree of motion blurring and contrast loss depends on the lesion size and location.

In order to contribute for the full understanding of this problem, the GATE Monte Carlo platform was used to model the microPET® FOCUS 220 system and the MOBY phantom to produce realistic simulated mouse scans. GATE is a well-validated and very versatile application for Monte Carlo simulations in emission tomography that can be used for highly realistic simulations. MOBY was developed to provide a realistic and flexible model of the mouse anatomy and physiology to be used in molecular imaging research.

2. Material and methods

2.1 The GATE platform

GATE is a Monte Carlo simulator (object-oriented simulation platform) based on Geant4 libraries (a generic Monte Carlo code), providing a scripting interface with a number of advantages for the simulation of Single Photon Emission Computed Tomography (SPECT) and PET systems, including the description of source decay phenomena, moving detector components and time management (Jan et al., 2004a). Since the code is based on Geant4, it profits from the validation of the underlying physics components including testing from a very large scientific community. At the same time, the scripting interface provides a convenient platform for most of the users to create their own simulation of emission tomography experiments and complicated emission tomography system designs.

The use of GATE facilitates the description of the different components necessary for the accurate modeling of a PET system, starting from the geometry configuration, up to the creation of a processing chain for the detected events. Analytical phantoms can also be defined through the use of these basic structures, while voxelized sources can be equally employed in order to represent realistic patient imaging conditions. The physics processes are based on Geant4 libraries including the modeling of radioactive source decays and particles interactions for standard and low energies. Users may also interactively select which gamma-ray interactions should be considered (photoelectric effect, Compton and Rayleigh scattering, and gamma-ray conversion), and may specify the energy cuts applied to the production of secondary gamma-rays and electrons. In addition, Geant4 material libraries in combination with user defined material tables are used to cover all of the object compositions necessary for the modeling of a system. A number of modules are available for modeling the detection process, going from the detection of the gamma-rays by the scintillating crystals (singles) to the detection of coincidences in PET. Simulation data results may be stored into multiple output files with different file formats. Time-dependence is taken into account at all steps of the simulation, so that realistic simulations of the acquisitions count rates and source decay can be achieved under dynamic configurations (e.g. rotation detectors or evolving bio-distributions).

2.2 Modeling the MicroPET® FOCUS 220

The microPET® FOCUS 220 system is a commercial scanner consisting in 4 detector rings: each ring is made of 42 detector blocks (Tai et al., 2005). Each detector block is composed of a matrix of 12×12 LSO crystals with the dimensions 1.5×1.5×10.0 mm^3. Its axial Field of View (FOV) is 7.6 cm and has a diameter of 26.0 cm. The FOCUS system has a volume resolution of 2.5 µL and an absolute sensitivity of 3.4%, both measured at the center of the FOV. The system is suitable for acquiring high-resolution images of small animal as rodents (mice and rats) and primates (macaque and small baboon).

The microPET® Focus 220 system was simulated in order to validate the use of GATE in the simulation of small animal PET. In order to do this, a model of the detection system and its geometry was developed. The accuracy of the developed detection model was tested through the comparison of simulated and measured results obtained from the FOCUS system for a number of performance protocols including spatial resolution, counting rate and contrast. Time dependence was introduced as a new feature to work with small animal imaging simulations. The geometry description of the microPET® scanner is illustrated in Fig. 1.

Accuracy and variability of quantitative values obtained for mouse imaging using the Focus system can be found in (Jan et al., 2004b).

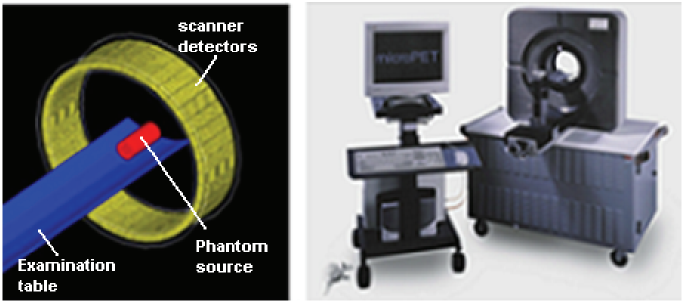

Fig. 1. MicroPET® FOCUS 220 geometry modeled by GATE (left) and the real system (right).

2.3 The MOBY phantom description within GATE

The MOBY mouse phantom combines the realism of a voxelized phantom, with the flexibility of a mathematical phantom, based on non-uniform rational B-splines (NURBS)

(Segars et al., 2004). The organ shapes are modeled with NURBS surfaces, widely used in three dimensional computer graphics to accurately describe complex 3D surfaces, providing the foundation for a realistic model of the 3D mouse anatomy. The phantom software could generate voxelized representations of the mouse anatomy at any user-defined resolution. Also, organs can be set to different tissue resolutions. The execution of the MOBY program generates 3D voxelized attenuation coefficient phantoms and 3D voxelized emission phantoms. These voxelized representations can be used as input in the GATE Monte Carlo platform.

The default whole body MOBY phantom consists of a matrix of 128×128×448 cubic voxels with 0.25 mm sides. We applied a resampling on the default MOBY matrix to reduce the voxel number to 40×40×124 voxels with a voxel unit size of 0.5×0.5×0.5 mm^3. This allowed to significantly reduce the computational time resulting from the particle tracking inside the simulated volume and took into account the spatial resolution of the scanner. The MOBY phantom includes 4D models of the mouse's cardiac and respiratory motions. Both motions were parameterized allowing changes on magnitude or rates of each motion to simulate many different variations, normal and abnormal. The MOBY respiratory motion was set up to be dependent on two time varying parameters: the change in the height of the diaphragm ($\Delta_{\text{diaphr.}}$) and the amount of chest expansion ($\Delta_{\Delta P}$). In the default MOBY configuration, the extent of diaphragmatic motion for normal breathing is set to be 1.0 mm while the chest expansion is 0.7 mm. These values correspond to a respiratory cycle with a period of 0.37 s. We manipulated these parameters to produce a "stress breathing" condition, in order to reproduce the respiratory motion of a mouse during a typical PET examination: the $\Delta_{\text{diaphr.}}(t)$ was set to 6.0 mm and the $\Delta_{\Delta P}(t)$ was defined to 4.2 mm.

A spherical lung lesion was implemented in the middle region of the left lung and its motion modeled as a function of the non-normal tidal breathing condition. The motion of a specific spot of the lung is modeled as a two-way motion between two points in space, with same cycle of the diaphragm movement.

For a respiratory cycle with a typical period of 0.37 s, the diaphragm motion can be decided by:

$$\Delta_{diaphr.}(t)=\begin{cases} 0.5mm\cos\left(\dfrac{\pi}{0.16}t\right)+0.5 & 0\le t\le 0.16s \\ 0.5mm\cos\left(\dfrac{\pi}{0.24}(0.4-t)\right)+0.5 & 0.16\le t\le 0.4s \end{cases} \tag{1}$$

The $\Delta_{\Delta P}(t)$ diameter of the chest was assumed to change a maximum of *N* mm's sinusoidally as shown in Equation:

$$\Delta_{\Delta P}(t)=\begin{cases} -\dfrac{N}{2}\cos\left(\dfrac{\pi}{0.16}t\right)+\dfrac{N}{2} & 0\le t\le 0.16s \\ -\dfrac{N}{2}\cos\left(\dfrac{\pi}{0.24}(0.4-t)\right)+\dfrac{N}{2} & 0.16\le t\le 0.4s \end{cases} \tag{2}$$

The *N* parameter was adjusted according to the total amount of volume change in the lungs (0.15 mL for normal tidal breathing in the mouse).

Each respiratory cycle was divided into *N* bins (temporal frames), and one phantom was created for each of the *N* instances of the respiratory cycle. Based on Equations (1) and (2), a set of 10 temporal frames (gates) of 0.037 s was generated over a complete respiratory cycle of 0.37 s in addition to a non-gated data set. The 10 respiratory gated images were produced by the MOBY program for 10 different position of one respiratory cycle. The first 5 images correspond to the inhalation and the other 5 images to the exhalation process respectively. The modified MOBY phantom and the parameter curves for both respiratory and lesion motion are illustrated in Fig. 2 and Fig. 3.

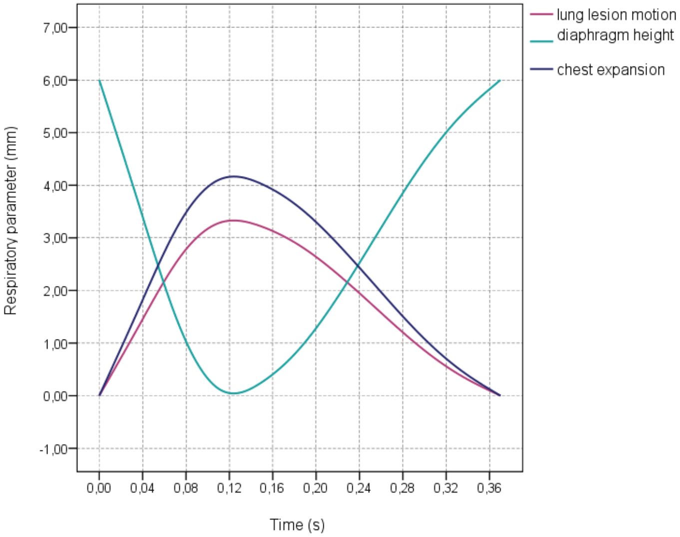

Fig. 2. Parameter curves and lesion motion for the “stress” breathing condition in the MOBY phantom.

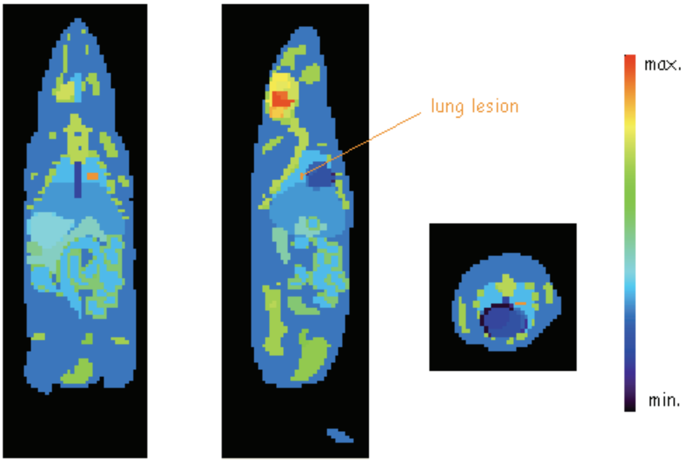

Fig. 3. Slices of the emission map of the MOBY phantom including a spherical lesion in middle region of the left lung, generated by the MOBY program.

For the studies without the inclusion of respiratory motion, simulations were carried out approximating clinical acquisitions of 15 minutes (last frame of a FDG acquisition) in order to provide whole-body images of variable statistical quality. For the simulations with respiratory motion, the acquisition time used in static simulation, T_{acqTot}, was divided by the number of respiratory cycles, N_{cycles}, and the number of bins, N_{bins}, per respiratory cycle to obtain the acquisition time at one instance (bin) of the respiratory cycle, T_{acqBin}:

$$T_{acqBin} = \frac{T_{acqTot}}{N_{cycles} N_{bins}} \tag{3}$$

In this way the total acquisition time remains the same for simulations with or without the inclusion of respiratory motion.

2.4 Metabolic imaging using FDG

The *2-Deoxy-[18F]fluoro-D-glucose* (FDG) is the most common radiotracer used for the study of cancer in the clinical setting. FDG is an analog of glucose and is taken up by living cells through the normal glucose pathway.

Tumor imaging with FDG is based on the fact that malignant tumors with high metabolic rates take up greater amounts of glucose and FDG than surrounding tissues (Couturier, 2004; Larson & Schwartz, 2006).

A dynamic whole body mouse FDG exam was used to generate an emission map that consist of a matrix of 104×61×95 voxels, which are of 0.46 mm along the *x* and *y* axis, and 0.80 mm along the *z* axis. The mouse was injected with an activity of 220 mCi and scanned during 90 minutes. Data was binned into 18 frames (5×60 s; 5×120 s; 3×300 s; 3×600 s; 2×900 s).

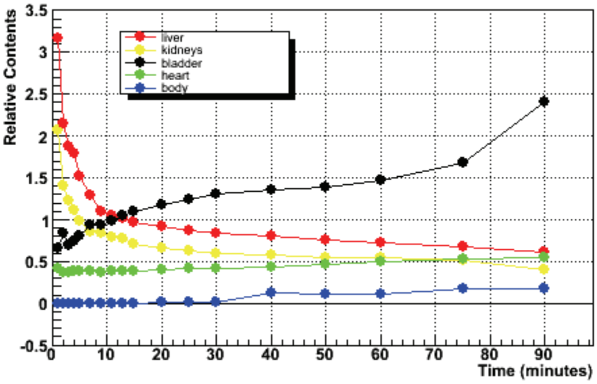

Fig. 4. Measured TACs used as input for the FDG uptake simulation.

The microPET images were employed in order to accurately model the variable FDG distributions. The FDG biodistribution is defined by the Time Activity Curves (TACs), which are assigned to different body structures. The dynamic FDG mouse exam was used to compute the FDG biodistribution, needed to set the activity distribution in each organ at each point of time in the simulation studies performed. Regions of Interest (ROIs) were drawn around the bladder, heart, liver, kidneys and whole body. The activity in each ROI was normalized to the total body activity in order to obtain a relative concentration in each organ at each time point. Fig. 4 shows the TAC for each organ at each time frame. The TACs for the function model of the FDG tracer are used to set the input activity function in each structure for the MOBY phantom.

2.5 Simulation and reconstruction set-up

In order to evaluate the effect of the respiratory motion in 3D and 4D microPET images, a set of static (non-gated MOBY data set without any motion associated) and dynamic (gated MOBY data set, where respiratory and lesion motions are present) FDG simulations were performed. Different lesion diameter (0.75 mm, 1.0 mm, 1.25 mm, 1.5 mm and 2.0 mm) were considered as well as different activity uptakes of FDG (0.01 μCi, 0.03 μCi, 0.05 μCi, 0.08 μCi, 1.08 μCi and 1.35 μCi), for the last time frame.

The gated and non-gated MOBY emission maps are integrated into GATE as voxelized sources to assign the activity to different anatomical structures, in order to obtain static and dynamic emission data sets.

The activity distribution in all of the other organs was defined according to the last acquisition time frame for an FDG exam (determined with a typical mouse FDG-PET exam). The concentration activity of the last frame (900 s of acquisition time) corresponds to a 131 μCi.

The FDG biodistribution was defined by the TACs obtained from real whole-body mouse PET exams, as described previous. The activity distribution, within the MOBY phantom, was set according to the activity distribution assigned to the different whole body structures for the FDG radiotracer. In all simulation protocols physical effects like positron range, gamma accolinearity and tissue attenuation were not taken into account in order to obtain the "best case scenario", which could be used as defining the optimal results that we could obtain with a dedicated scanner and a specific radiotracer. Simulated data were rebinned with the Fourier Rebinning algorithm (FORE) and reconstructed using the OSEM2D method (16 subsets and 4 iterations).

2.6 Evaluation of the respiratory motion in lung lesion quantification

With the goal of better understanding the effect of the respiratory motion we have investigated the combined effects of target size, target-to-background activity concentration ratio and extent of respiratory motion on signal recovery of spherical lesions (targets) in 3D and 4D microPET images.

Sets of static (non-gated MOBY data set without any motion associated) and dynamic (gated MOBY data set, where respiratory and lesion motions are present) FDG simulations were performed. Different lesion diameters (0.75 mm, 1.0 mm, 1.25 mm, 1.5 mm and 2.0 mm) were considered as well as different activity uptakes of FDG (0.1 mCi, 0.3 mCi, 0.5 mCi, 0.8 mCi, 1.08 mCi and 1.35 mCi), for the last time frame. The gated and non-gated MOBY emission maps are integrated into GATE as voxelized sources to assign the activity to different anatomical structures, in order to obtain static and dynamic emission data sets.

The activity distribution in all of the other organs was defined according to the last acquisition time frame for an FDG exam (determined with a typical mouse FDG PET exam). The concentration activity of the last frame (900 s of acquisition time) corresponds to 131 mCi.

The FDG biodistribution was defined by the TACs obtained from real whole-body mouse PET exams, has described previously. The activity distribution, within the MOBY phantom, was set according to the activity distribution assigned to the different whole body structures for the FDG radiotracer. In all simulation protocols, physical effects like positron range, gamma accolinearity and tissue attenuation were not taken into account in order to obtained the "best case scenario", which could be used as defining the optimal results that could be obtain with a dedicated scanner and a specific radiotracer.

2.7 Data analysis

Detection in PET images strongly depends on the ability to recognize the signal pattern in the presence of noisy background that in turn, is limited by the capability of the imaging system to detect objects with very low contrast relatively to the background level and to spatially resolve a focal uptake. In the following paragraphs, the general methodology to evaluate the signal detection capability of an imaging system is presented. Although only the basic concepts on signal detection theory will be introduced, its description is important to contextualize the adopted analysis using the simulated data acquired with the microPET® Focus 220 scanner model.

The spatial resolution was measured by the Full Width at Half Maximum (FWHM). The FWHMs of reconstructed lesion images were determined along the direction of lesion movement due to respiratory motion. The image statistics were evaluated by calculating the signal-to-noise ratio (SNR) and contrast-to-noise ratio (CNR). The SNR is defined as the ratio of the average activity concentration measured in the target to the standard deviation. The higher the SNR, the less obtrusive the noise is. SNR is often defined as:

$$SNR = \frac{T}{\sigma_T} \tag{4}$$

The CNR was calculated as:

$$CNR = \frac{T - B}{\sqrt{\sigma_T^2 + \sigma_B^2}} \tag{5}$$

where T and B are the average activity concentrations measured in the target (lung lesion) and background region in the reconstructed image, respectively. $\sigma_{T,B}^2$ are the variances of these activities (Lartizien et al., 2004).

In general, the "quality" of an image can be described (quantitatively) by its SNR. The SNR directly affects diagnostic and quantitative accuracy. In essence, then, a major goal of nuclear medicine equipment is to maximize the SNR in an image. The CNR refers to the ability in PET to distinguish between various contrasts in an acquired image and the inherent noise in the image. The mean signal recovery of SNR and CNR were evaluated as a function of the lesion size and the lesion activity uptake, using Equations (4) and (5).

The target-to-background ratio (TBR) is defined as the relation between the lesion activity to the background activity concentration. The TBR values are computed using the following relation:

$$TBR = \frac{T}{B} \tag{6}$$

The data recorded from the ROIs were used to compute the contrast (C) and the volume recovery coefficient (VRC). The evaluation of the contrast indicates how reliable the reconstructed image would be for lesion detection tasks in real situations. This result in the ability to evaluate the reconstruction algorithm used to recover a certain simulated contrast between a lesion and a background. The contrast between the simulated lesions and the surrounding organs in the reconstructed images was computed using the expression:

$$C = \frac{T - B}{T + B} \tag{7}$$

where T was the mean activity in the simulated spherical lesion ROI and B was the mean activity in the background region ROIs. Higher contrast values are often related with noisier images. In practice, this contrast is provided by the radiotracer's distribution. The goal of the imaging system is to preserve this contrast in the image. Contrast is maintained by avoiding blurring, which smears counts from higher activity regions into lower activity regions (and vice versa), thus reducing image contrast. In this way, spatial resolution and contrast are closely linked.

In order to determine temporal resolution, the VRC was defined as:

$$VRC = \frac{V_{measured}}{V_{true}} \tag{8}$$

where $V_{measured}$ is the measured lesion volume and V_{true} is the real lesion volume. To perform data analysis, and quantify VRC values, we have drawn a volume of interest (VOI) around the centroid of each lesion. The size of the drawn VOI depends on the lesion size, in order to include as many voxels as possible, to keep a good statistic, and, at the same time, to include only voxels that corresponded to the lesion. For each VOI we calculated the average number of counts in each voxel. Background values were obtained by drawing and merging circular VOIs around each lesion (within the surrounding soft tissues: lung and liver regions) and by calculating the average number of counts and the corresponding standard deviation within. These data was also used to calculate the mean percent error in the volume for each lesion. The mean percent error between the estimated volume and the true volume of the spherical lesions was given by:

$$\%\,error = \frac{V_{measured} - V_{true}}{V_{true}} \tag{9}$$

3. Results

3.1 Quantification considerations

Detection in PET images At the beginning of this discussion we stated that the results obtained for the higher diameter lesions (1.25 mm, 1.5 mm and 2.0 mm) in the dynamic mode (gated images) are not show due to lesion blending into the liver. Additionally, due to the limited spatial resolution of the scanner used the results obtained for the smallest lesion (0.75 mm) may be compromised by a decrease in the sensitivity of detection and thus statistics could not be accurately measured. Due to this, to evaluate the effects produced by the respiratory motion we choose to use the 1.0 mm lesion.

Concerning data analysis, a selected lesion ROI for each particular case was used to estimate T (average activity concentrations measured in the lesion) when positioned over a background region. In the present analysis, the mean lung lesion activity T was computed as the average pixel intensity in the spherical ROI located at the lesion. The ROIs were all extracted from transaxial slices of the MOBY phantom passing through the different planes containing the lesion activity. The mean background activity B was estimated as the average pixel intensity within ROIs projected into reconstructed images without the lesion data added, however surrounding the lesion location. The placement of the lesion ROI for a 1.0 mm diameter lesion and background ROIs is illustrated in Fig. 5.

Fig. 5. Sagital slices through the MOBY phantom containing a 1.0 mm diameter lung lesion or only background, illustrating the placement of the background and lesion ROIs used for data analysis.

The statistical errors measured as the ratio standard deviation over mean for all ROIs considered for each lesion diameter, as function of the activity defined, are represented in Table 1. We found higher values in higher activity concentrations. This Table suggests that for the smaller lesion sizes (0.75 mm and 1.0 mm diameter) we have compromised results when compared to the statistical errors obtained for the other lesion sizes due to limited FOCUS system resolution. In addition, lower activity concentrations (0.1 mCi and 0.3 mCi) show the same behavior because lower activity concentrations significantly deteriorate the lesion signal recovery. The statistical errors for the ROIs considered in static simulation were found to be 18.92% and 22.44% for the dynamic simulations.

Activity (µCi)	Static Simulations					Dynamic Simulations
	Lesion Diameter					
	0.75 mm	1.0 mm	1.25 mm	1.5 mm	2.0 mm	1.0 mm
0.1	12.26%	21.0%	20.58%	14.56%	18.91%	11.81%
0.3	17.16%	33.92%	25.82%	16.98%	19.41%	9.11%
0.5	20.22%	43.43%	33.66%	31.72%	24.39%	11.88%
0.8	22.80%	49.65%	39.39%	37.25%	27.64%	14.54%
1.08	24.68%	51.74%	41.85%	40.35%	32.76%	19.54%
1.35	24.82%	55.46%	43.72%	42.67%	37.73%	20.71%

Table 1. Statistical error obtained for the defined ROIs in the lung lesion implementation in the MOBY phantom, from the static and the dynamic simulation modes.

3.2 Motion blurring versus spatial resolution

"Best case scenario" images are presented in Fig. 5 and Fig. 6, from static (non-gated data, without motion involved) and dynamic simulated data (gated data, where respiratory and lesion motions are present).

From Fig. 6 and Fig. 7 differences between the non-gated data set (static simulation) and the gated data set (dynamic simulation) can be seen. The extent of respiratory motion is evident between the 1st and the 10th frames in Fig. 7. The coronal slices shows the realistic motion of the various structures present in the thorax and upper abdomen due to the lungs expansion and contraction for the non normal tidal breathing configuration.

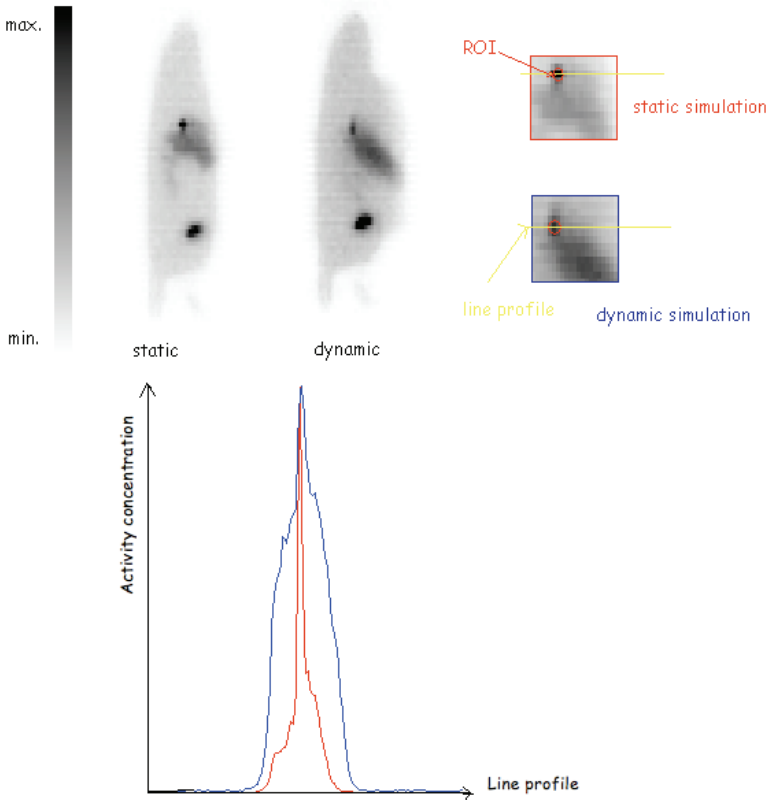

Fig. 6. Sagital slices, of the reconstructed MOBY phantom, for a static acquisition, where no motion was simulated, and for the simulation of a dynamic acquisition, where respiratory and lesion motions were considered, with a lung lesion of 1.0 mm diameter and an FDG uptake of 0.5 mCi. The maximum concentration profiles from 3D and 4D simulated exams: where the blurring or smearing effect induced by respiratory motion are represented in the right.

From the visual inspection of the static image, in Fig. 6, the lesion is clearly shown, keeping its spherical shape. However, for the dynamic image, in the same Figure, the lesion appears blurred and elongated as a consequence of the breathing movement. Consequently, respiratory motion may preclude the accurate detection of small lung lesions.

The motion vector defined in section 2.3 (Equation (1)) indicates more motion blurring within the transaxial plane than along axial (z) direction. Fig. 8 shows the difference of blurring along different directions. This result also indicates, due to respiratory motion, that a sphere lesion can be blurred to a shape with different size in different directions in 3D space. Additionally, the extent of blurring along different directions will depend on the motion vector at the position in the lung.

Fig. 7. Coronal slices of the MOBY phantom corresponding to the simulation of a “stress” condition breathing motion including a lung motion lesion of 1.5 mm diameter and an FDG uptake of 1.35 mCi. These coronal slices represent one respiratory cycle for an FDG exam in the last time frame. The dynamic 3D emission assumed an event collection during 900 s, where 5.65×10^9 particles were generated.

Fig. 8. Transaxial, coronal and sagital slices of the reconstructed lung lesion, in the MOBY phantom, with 2.0 mm diameter and an FDG uptake of 0.8 mCi. No motion was simulated.

The image spatial resolution was parameterized by the FWHM of Gaussian fits of the profiles taken over all lesions in the reconstructed images of the MOBY phantom. The results obtained for the static acquisitions are illustrated in Fig. 9. Spatial resolution improves most significantly for the smallest lesion diameter and at the same time for higher activity uptakes.

Fig. 10 shows the axial resolution of the lesion with 1.0 mm diameter for static and dynamic acquisitions, as a function of different FDG uptakes. It demonstrates that the blurring effect is lower for static acquisitions. It also demonstrates that when the FDG uptake increases the blurring decreases for dynamic and static acquisitions and consequently improves spatial resolution.

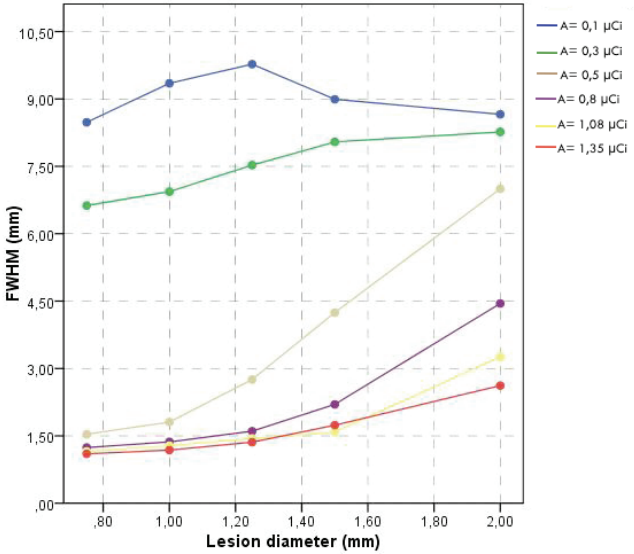

Fig. 9. FWHM of the line spread function through the lesion centroid as a function of the lesion diameter defined for the static acquisitions schemes.

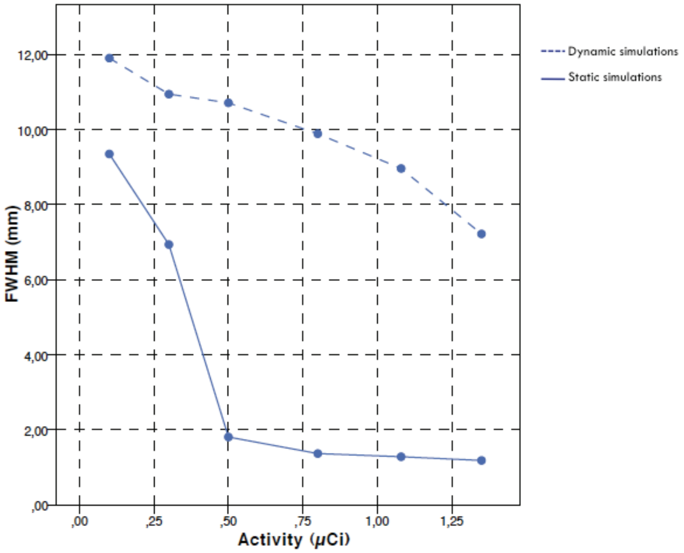

Fig. 10. FWHM of the line spread function through the lesion centroid as a function of the FDG activity defined for static and dynamic acquisitions schemes, for the 1.0 mm diameter lesion. Data from dynamic acquisitions are represented by dashed curves and static acquisition data are represented by solid curves.

3.3 Lesion detectability

Signal-to-noise (SNR) ratios are indicators of the visual utility of an image for detection purposes. The SNR directly affects diagnostic and quantitative accuracy (Sain & Barrett, 2003). The SNR describes the relative "strength" between the desired information and the noise in the image. The higher the SNR, the less obtrusive the noise is. The value SNR = 5 is the conventional value of detectability used in radiology, and as also been used in emission tomography images. Lesions for which $T-B>5\sigma_T$ can be considered 100% visible (Cherry et al., 2003; Graham & Links, 2007). SNR values for the lower lesion activity concentration are in the vast majority of situations higher than the 100% detectability limit.

Fig. 11 show that the SNR depends strongly both on the lesion diameter and on the activity concentration. Nevertheless, the plots presented show that, for the highest activity values, most of the lesions converge to SNR values that are below the line of 100% visibility. In the case of higher activity concentrations, the smallest lesion diameter tend to converge to SNR values close to the 100% detectability line against SNR values that are significantly below that value for highest lesion diameter. However, according to the reconstructed images, the lesions with the considered diameters for all activity concentration ratios are all observable by visual inspection (some difficulties appear for the smallest lesions with lower activity concentrations, and the largest due to the lesion blending in the surrounding organs). This seems to indicate that the SNR = 5 criterion, from conventional radiology, might not be a good detectability criterion for emission tomography images. Keeping this in mind, we will, nevertheless, use this criterion as a reference for the quality of the images with respect to its SNR ratio.

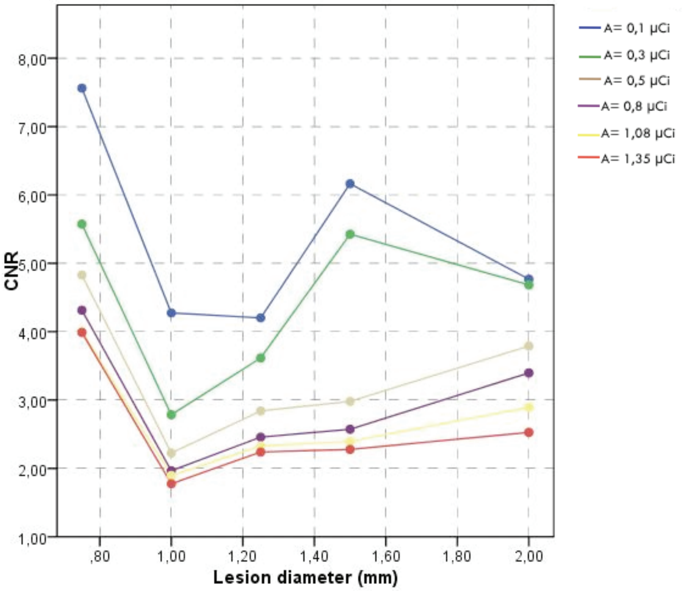

Fig. 11. SNR of the 0.1 mCi, 0.3 mCi, 0.5 mCi, 0.8 mCi, 1.08 mCi and 1.35 mCi FDG uptakes for the spherical lesions as a function of the lesion diameter. Results obtained for the static simulations.

Despite of the increase in the mean signal recovery, as a function of the FDG concentration increase, the standard deviation had also a significant increase. This result in a decrease of the SNR recovers values. We get the same behavior for the CNR values as a function of the activity concentration. These results can also be explained through the results obtained for the spatial resolution versus the motion blurring.

In respect to the CNR, when the size of a lesion is substantially larger than the limiting spatial resolution it can influence the detection ability, especially if the lesion has low contrast. The CNR is displayed in Fig. 12 as a function of the lesion diameter, and for different activity uptakes. Overall, CNR improves significantly as lesion contrast decreases and lesion size increases.

We need to have into account the same line of the results inspection: caused by the small size of lesions relative to scanner resolution (partial-volume effect) we got higher CNR values for the smallest lesion.

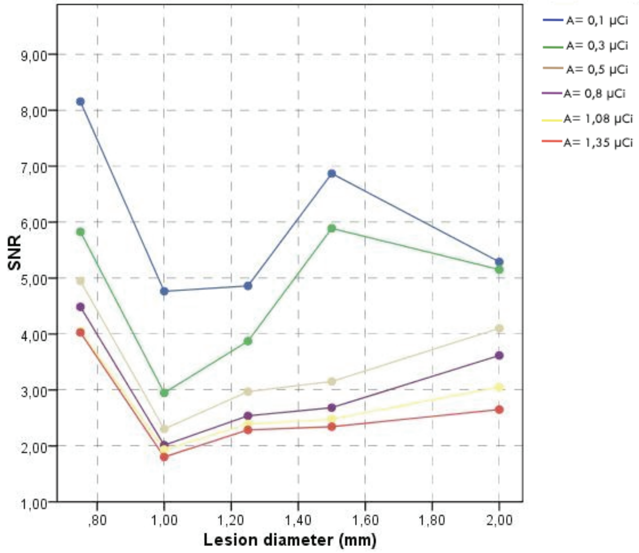

Fig. 12. CNR of the 0.1 mCi, 0.3 mCi, 0.5 mCi, 0.8 mCi, 1.08 mCi and 1.35 mCi FDG uptakes for the spherical lesions as a function of the lesion diameter. Results obtained for the static simulations.

Table 2 summarizes SNR and CNR values in the lesion with 1.0 mm diameter as a function of the FDG activity concentration. The first columns show the CNR and the SNR from the non-gated images of the phantom in a static mode. The other results correspond to data obtained from the gated images of the phantom in the dynamic mode. The dynamic simulations results in larger overestimations of SNR due to poor counting statistics and high image noise. This effect is more significant as the lesion activity concentration decreases, as it is shown in Table 2. However, the same table shows a slight improvement in CNR recovery for the dynamic acquisitions as the lesion activity increases. Respiratory motion has less of an effect on the peak lesion signal and thus could explain the improvement on the dynamic CNR results.

We expected improvements on the SNR and the CNR data as a function of the increase of the FDG activity (higher activities always provide better SNR and CNR). This is due to the fact that we defined the lesion motion as a function of the no normal tidal breathing and thus with a largest magnitude of motion. Because there is a higher motion in this condition then it is expected that we will get an improved signal recovery for the lower contrast lesions. As discussed before, the values obtained for the other dynamic acquisitions sets are quantitatively changed due to the lesion blending into the liver (in the case of the largest diameter lesions) and are not used in the comparative set. We decided to remove the comparative set for the smallest lesion because the statistical results may be compromise by the limited spatial resolution of the microPET® FOCUS 220.

	Static Simulations		Dynamic Simulations	
Activity (µCi)	CNR	SNR	CNR	SNR
0.1	4.274	4.764	0.213	8.465
0.3	2.785	2.948	2.405	10.975
0.5	2.225	2.303	2.407	8.419
0.8	1.966	2.014	2.920	6.880
1.08	1.897	1.933	2.823	5.117
1.35	1.766	1.803	2.968	4.829

Table 2. SNR and CNR values in the lesion with 1.0 mm diameter as a function of the FDG activity concentration. The first columns show the CNR and the SNR from the images of the phantom in a static mode. The other results correspond to data obtained from the images of the phantom in the dynamic mode.

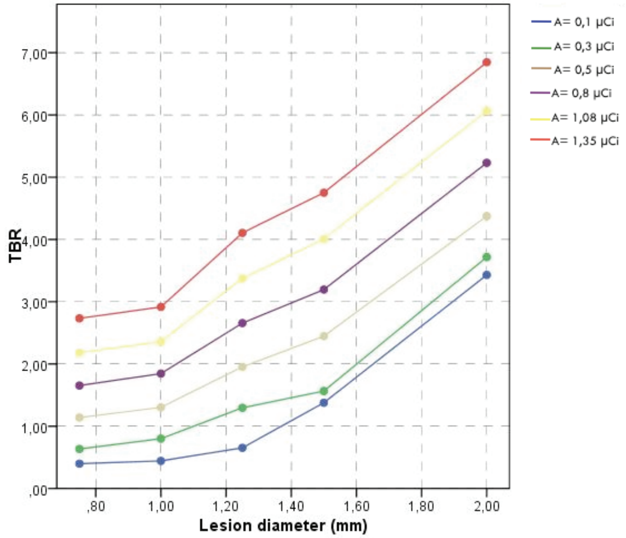

Fig. 13. TBR of the 0.1 mCi, 0.3 mCi, 0.5 mCi, 0.8 mCi, 1.08 mCi and 1.35 mCi FDG uptakes for the spherical lesions as a function of the lesion diameter. Results obtained for the static simulations.

Fig. 13 illustrates the relationship between contrast and activity concentration, TBR, as a function of the lesion diameter. The higher the contrast the higher is the detectability. Fig. 14 shows the TBR plot for a set of dynamic and static acquisitions as a function of the FDG activity concentration, for the lesion diameter of 1.0 mm. The curves show that the TBR increases as the activity concentration increases. Moreover, and as expected, the figure also illustrates that we achieved lower TBR values for the images of the moving lesions.

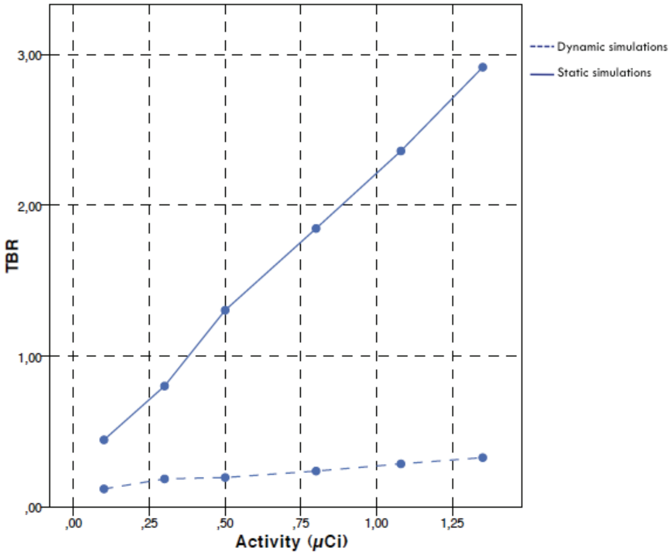

Fig. 14. TBR of a set of a dynamic and a static acquisition as a function of the FDG activity concentration for the 1.0 mm diameter lesion. Data from dynamic acquisitions are represented with the dashed curve and static acquisition data are represented by the solid curve.

3.4 Evaluation of the contrast and volume recovery coefficient

The Fig. 15 shows the trends of the contrasts, in the static acquisition simulations, against lesion diameter, for all the lesion activity uptakes considered. As it can be seen in these plots, the contrast values obtained in these studies are always high, even for the smallest lesion diameter. These plots highlight the fact that the contrast depends more strongly on the lesion diameter than it depends on the lesion to background considered. In fact, for a given diameter, the contrast is approximately the same for all the different activity uptakes. The strong dependence on lesion diameter illustrates a significant partial volume effect.

Fig. 16 illustrates the contrast of a set of dynamic and static acquisitions as a function of the FDG activity concentration for the 1.0 mm diameter lesion. We found higher contrast values from the dynamic data against the static data. We expected that the motion decrease the contrast in the reconstructed images, while images from static acquisitions can largely recover the signal lost due to motion. These results are influenced from the ROIs defined in the background level. However, the mean signal recover is higher in static data when compared to the dynamic data. These results suggest that the ROIs approach for the background level used probably was not the best choice (despite of the approach used in pre-clinical practice).

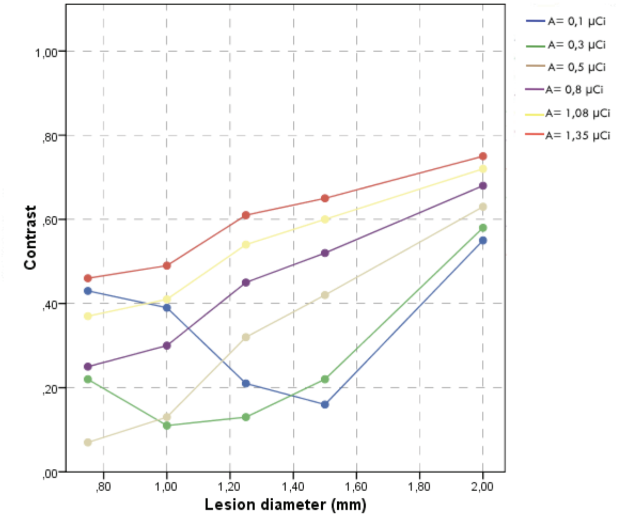

Fig. 15. Contrast of the 0.1 mCi, 0.3 mCi, 0.5 mCi, 0.8 mCi, 1.08 mCi and 1.35 mCi FDG uptakes for the spherical lesions as a function of the lesion diameter. Results obtained for the static simulations.

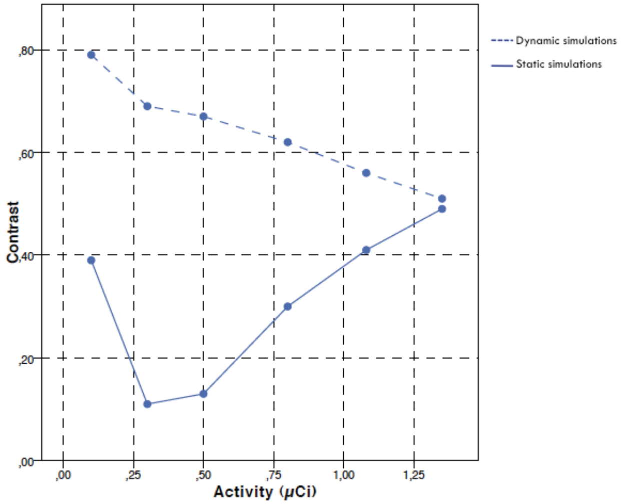

Fig. 16. Contrast of a set of dynamic and static acquisitions as a function of the FDG activity concentration for the 1.0 mm diameter lesion. Data from dynamic acquisitions are represented by the dashed curve and static acquisition data are represented by the solid curve.

Table 3 summarizes the VRC as a function of the lesion diameter, for static and dynamic acquisitions. As expected, with dynamic acquisitions the volumes of sphere were overestimated due to the smearing effect resulting from motion. For static acquisitions the VRC values are close to 1.0, which means that values were correctly recovered. The table also shows the mean percent errors in volume estimates measured on the simulated lesions as a function of the real lesion volume.

Lesion diameter (mm)	Static Simulations		Dynamic Simulations	
	VRC	% error	VRC	% error
0.75	1.629	61.30	3.259	225.88
1.0	1.120	12.02	2.930	192.98
1.25	1.098	9.83	N/A	N/A
1.5	0.987	1.27	N/A	N/A
2.0	0.995	0.54	N/A	N/A

Table 3. VRC in the static and dynamic acquisitions as a function of the lesion diameter. The mean percent errors in volume estimates measured on simulated lesions as a function of the real lesion volume are also shown.

(Note: N/A - ″not available″ - is this context means that the VRC value was not possible to measure due to the blurring and to the smearing effect resulting from the respiratory motion.)

4. Conclusions and perspectives

The FWHMs of reconstructed lesion images were determined alongside with the direction of movement due to respiratory motion for static and dynamic acquisitions. The results demonstrate how the respiratory motion would affect the blurring of a lung lesion along the direction of movement.

As expected, contrast-to-noise ratio (CNR) recovery improves for static acquisitions. The static images have a slightly greater CNR recovery compared to the dynamic images, which is due to the loss of resolution in the motion images. CNR recovery also improves as lesion size increases and lesion contrast decreases.

The results illustrates that the signal-to-noise ratio (SNR) deteriorate for motion data. Results for higher diameter lesions in the lung were influenced by lesion blending into the liver. However, results for the 1.0 mm lesion shown better SNR data induced by the respiratory motion. Concerning the static acquisitions we found better SNR for lower FDG uptakes and higher lesion sizes. The contrast depends more strongly on the lesion diameter than it depends on the lesion to background considered. Better temporal resolution (volume recover) was found in the non-gated data.

As discussed before, respiratory motion leads to reduced contrast and quantitative accuracy in terms of recovered contrast activity concentration and functional volumes. Several methodologies proposed for reducing the effects of respiratory motion have been based on the development of respiratory-gated acquisitions (Visvikis et al., 2006; Nehmeh et al., 2002; Dawood et al., 2006; Detorie & Dahlbom, 2006; Lamare et al., 2007a; Dawood et al., 2008; Bettinardi, 2009; Lamare et al., 2007b; Detorie & Dahlbom, 2008). However, in general, 4D PET images have low counting statistics and high image noise compared to static 3D PET images. Since the same number of coincidence events in 3D PET is divided into many different respiratory phase bins or time frames, the number of coincidence events per image bin is considerably reduced. This leads to higher image noise in 4D PET images, resulting in an even lower SNR of the reconstruction. Therefore, there is a trade-off between image noise and temporal resolution. Long duration time per frame gives low noise but blurred images resulting from the loss of temporal resolution (Park et al., 2008; Zhu et al., 2002). In order to determine the effect of the number of gating bins on image noise and temporal resolution, sets of 4D simulations will be performed for the MOBY phantom following the same line of reasoning of these studies.

Some other limitations of our research are related to the phantom's anatomy and breathing cycle. In future studies different phantoms anatomy can improve our quantitative evaluation. In our work, we produced a stress breathing condition on the respiratory motion cycle of the phantom, whereas variations in respiratory cycle from an animal to another and in time may also influence the observed effects. Moreover, variations in the amplitude of the diaphragm motion also influence the results. A reference to a real examination can be helpful to compare the results obtained. Therefore, there is still the need for a method that takes into account the effect of respiratory motion without, at the same time, affecting the quantification analysis on the reconstructed images. For that reason, this work is being complemented by accessing the impact of such motion in the quantification analysis using a dynamic VOI, placed around the centroid of each lesion, in 4D imaging studies.

This research contributes to evaluating the respiratory motion effect in the quantification of microPET images. A complete evaluation should also consider real dynamic FDG examinations that need to be compared against the results presented in this thesis. Moreover, the production of realistic images, where attenuation information (using the phantoms attenuation maps to set the different body structures and the correspondent attenuation information) and physical effects (using the isotope decay instead a gamma/gamma emission source) are included, was not done. Although this was not among the main goals of this work, its inclusion would allow evaluating the consequence of these physical effects on image sensitivity and quantification. Since the physical effects are not taken into account, further investigation is needed to accurately evaluate these effects on image quantification.

We have used the OSEM algorithm for image reconstruction with fixed parameters (16 subsets and 4 iterations). These parameters are normally used in pre-clinical standard protocols. However, there are several other image reconstruction algorithms and parameters including smoothing filters and the number of subsets and iterations that could affect the results (namely, lesion quantification may be inaccurate depending on the reconstruction algorithms used), but have not been addressed in this study. Further studies are required to investigate the effect of these parameters on signal and volume recovery.

In this research we have always used the same breathing condition to simulate respiratory motion.

However, image quantification is influenced by the amplitude and pattern of respiratory motion. This suggests that it may be beneficial to simulate different breathing motion conditions to obtain a reasonable estimate on image quantification under clinical conditions.

Background activity is unavoidable and it causes significant noise and contrast loss in PET images (Tai & Laforest, 2005). The effect of background activity concentration will be analyzed in the next phases of this research.

5. References

Andreo, P. (1991). Monte carlo techniques in medical radiation physics. Physics in Medicine and Biology, Vol. 36, No. 7, pp. (861–920).

Andreo, P., & Ljungberg, M. (1998). *Monte Carlo Calculations in Nuclear Medicine: Applications in Diagnostic Imaging*. Institute of Physics Publishing. Chap. General Monte Carlo Codes for use in Medical Radiation Physics, pp. (37–52).

Bettinardi, V. (2009). Number of partitions (gates) needed to obtain motion-free images in a respiratory gated 4D-PET/CT study as a function of the lesion size and motion displacement. *Medical Physics*, Vol. 36, No. 12, pp. (5547–5558).

Buvat, I., & Castiglioni, I. (2002). Monte Carlo simulations in SPECT and PET. *The Quarterly Journal of Nuclear Medicine*, Vol. 46, No. 1, pp. (48–61).

Buvat, I., Castiglioni, I., Feuardent, J. & Gilardi, M.-C. (2005). Unified description and validation of Monte Carlo simulators in PET. *Physics in Medicine and Biology*, Vol. 50, pp. (329–346).

Buvat, I., & Lazaro, D. (2006). Monte Carlo Simulations in Emission Tomography and GATE: an overview. *Nuclear Instruments and Methods in Physics Research A*, Vol. 569, pp. (323–329).

Chatziioannou, A. F. (2002). PET scanners dedicated to molecular imaging of small animal models. *Molecular Imaging and Biology*, Vol. 4, No. 1, pp. (47–63).

Cherry, S. R. (2004). In vivo molecular and genomic imaging: new challenges for imaging physics. *Physics in Medicine and Biology*, Vol. 49, pp. (R13–R48).

Cherry, S. R., & Gambhir, S. S. (2001). Use of positron emission tomography in animal research. *Institute for Laboratory Animal Research*, Vol. 42, No. 3, pp. (219–232).

Cherry, S. R., Sorenson, J. A., & Phelps, M. E. (2003). *Physics in Nuclear Medicine*. Saunders. Chap. Image Quality in Nuclear Medicine, pp. (253–272).

Couturier, O. (2004). Fluorinated tracers for imaging cancer with positron emission tomography. *European Journal of Nuclear Medicine and Molecular Imaging*, Vol. 31, No. 8, pp. (1182–1206).

Dawood, M., Lang, N., Jiang, X. & Schafers, K. P. (2006). Lung motion correction on respiratory gated 3D PET/CT images. *IEEE Transactions of Medical Imaging*, Vol. 25, No. 4, pp. (476–485).

Dawood, M., Buther, F., Jiang, X. & Schafers, K. P. (2008). Respiratory motion correction in 3D PET data with advanced optical flow algorithms. *IEEE Transactions on Medical Imaging*, Vol. 27, No. 8, pp. (1164–1175).

Detorie, N., & Dahlbom, M. (2006). Motion correction for respiratory gated PET images. *IEEE Nuclear Science Symposium Conference Record*, pp. (3273–3277).

Detorie, N. C., & Dahlbom, M. (2008). Quantitative evaluation of reconstruction algorithms for motion compensated PET. *Nuclear Science Symposium Conference Record*, pp. (5366–5372).

GATE. 2010. http://www.opengatecollaboration.org.

Graham, L. S., & Links, J. M. (2007). *Nuclear medicine and PET/CT: Technology and Techniques*. Mosby Elsevier. Chap. Instrumentation, pp. (59–104).

Jan, S., et al. (2004a). GATE: a simulation toolkit for PET and SPECT. *Physics in Medicine and Biology*, Vol. 49, No. 19, pp. (4543-4561).

Jan, S., Boisgard, R., Fontyn, Y., Eroukhmanoff, C., Comtat, C., & Trebossen, R. (2004b). Accuracy and variability of quantitative values obtained for mouse imaging using the microPET Focus. *Nuclear Science Symposium Conference Record*, Vol. 5, pp. (2934–2937).

Jan, S., Desbree, A., Pain, F., Guez, D., Comtat, C., Gurden, H., Kerhoas, S., Laniece, P., Lefebvre, F., Mastrippolito, R., & Trebossen, R. (2005). Monte Carlo simulation of the microPET Focus system for small rodents imaging applications. *IEEE Nuclear Science Symposium Conference Record*, Vol. 3, pp. (1653–1657).

Lamare, F., Carbayo, M. J. Ledesma, Cresson, T., Kontaxakis, G., Santos, A., Rest, C. Cheze Le, Reader, A. J., & Visvikis, D. (2007a). List-mode-based reconstruction for respiratory motion correction in pet using nonrigid body transformations. *Physics in Medicine and Biology*, Vol. 52, pp. (5187–5204).

Lamare, F., Cresson, T., Savean, J., Rest, C. Cheze Le, Reader, A. J., & Visvikis, D. (2007b). Respiratory motion correction for pet oncology applications using affine transformation of list mode data. *Physics in Medicine and Biology*, Vol. 52, pp. (121–140).

Larson, S. M., & Schwartz, L. H. (2006). ^{18}F-FDG PET as a candidate for qualified biomarker: Functional assessment of treatment response in oncology. *The Journal of Nuclear Medicine*, Vol. 47, No. 6, pp. (901–903).

Lartizien, C., et al. (2004). A Lesion Detection Observer Study Comparing 2-Dimensional Versus Fully 3-Dimensional Whole-Body PET Imaging Protocols. *Journal of Nuclear Medicine*, Vol. 45, pp. (714-723).

Ljungberg, M. (1998). *Monte Carlo Calculations in Nuclear Medicine: Applications in Diagnostic Imaging*. Institute of Physics Publishing. Chap. Introduction to the Monte Carlo Method, pp. (1–12).

Ljungberg, M. (2004). *Emission tomography: The fundaments of PET and SPECT*. Elsevier. Chap. Simulation Techniques and Phantoms, pp. (551–563).

Nehmeh, S. A., Erdi, Y. E., Ling, C. C., Rosenzweig, K. E., Schoder, H., Larson, S. M., Macapinlac, H. A., Squire, O. D. & Humm, J. L. (2002). Effect of respiratory gating on quantifying PET images of lung cancer. *Journal of Nuclear Medicine*, Vol. 43, No. 7, pp. (876–881).

Park, S.-J., Ionascu, D., Killoran, J., Mamede, M., Gerbaudo, V. H., Chin, L. & Berbeco, R. (2008). Evaluation of the combined effects of target size, respiratory motion and background activity on 3D and 4D PET/CT images. *Physics in Medicine and Biology*, Vol. 53, pp. (3661–3679).

Peter, J., Tornai, M. P., & Jaszczek, R. J. (2000). Analytical versus voxelized phantom representation for Monte Carlo simulation in radiological imaging. *IEEE Transactions on Medical Imaging*, Vol. 19, pp. (556–564).

Poston, J. W., Bolch, W., & Bouchet, L. (2002). *Therapeutic Applications of Monte Carlo Calculations in Nuclear Medicine*. Institute of Physics Publishing. Chap. Mathematical models of the human anatomy, pp. (108–132).

Riemann, B., Schafers, K. P., Schober, O., & Schafers, M. (2008). Small animal PET in preclinical studies: opportunities and challenges. *Quarterly Journal of Nuclear Medicine and Molecular Imaging*, Vol. 52, No. 3, pp. (215–221).

Rogers, D. W. O. (2006). Fifty years of Monte Carlo simulations for medical physics. *Physics in Medicine and Biology*, Vol. 51, pp. (R287–R301).

Rowland, D. J., & R., S. R. Cherry S. (2008). Small-animal preclinical nuclear medicine instrumentation and methodology. *Seminars in Nuclear Medicine*, Vol. 38, No. 3, pp. (209–222).

Sain, J. D., & Barrett, H. H. (2003). Performance evaluation of a modular gamma camera using a detectability index. *The Journal of Nuclear Medicine*, Vol. 44, No. 1, pp. (58–66).

Sang-June, P., et al. (2008). Evaluation of the combined effects of target size, respiratory motion and background activity on 3D and 4D PET/CT images. *Physics in Medicine and Biology*, Vol. 53, pp. (3661-3679).

Segars, W. P., et al. (2004). Development of a 4-D Digital Mouse Phantom for Molecular Imaging Research. *Molecular Imaging and Biology*, Vol. 6, No. 3, pp. (149-159).

Tai, Y.-C., & Laforest, R. (2005). Instrumentation aspects of animal pet. *Annual Review of Biomedical Engineering*, Vol. 7, pp. (255–285).

Tai, Y., et al. (2005). Performance Evaluation of the microPET FOCUS: A Third-Generation microPET Scanner Dedicated to Animal Imaging. *Journal of Nuclear Medicine*, Vol. 46, pp. (455-463).

Visvikis, D., Lamare, F., Bruyant, P., Boussion, N., & Le Rest, C. C. (2006). Respiratory motion in positron emission tomography for oncology applications: Problems and solutions. *Nuclear Instruments and Methods in Physics Research A*, Vol. 569, pp. (453–457).

Zaidi, H. (1999). Relevance of accurate Monte Carlo modeling in nuclear medical imaging. *Medical Physics*, Vol. 26, No. 4, pp. (574–608).

Zaidi, H. (2006). *Quantitative analysis in Nuclear Medicine Imaging*. Springer Publishing. Chap. Monte Carlo Modeling in Nuclear Medicine Imaging, pp. (358–390).

Zaidi, H., & Sgouros, G. (2002). *Therapeutic Applications of Monte Carlo Calculations in Nuclear Medicine*. Institute of Physics Publishing.

Zubal, I. G. (1998). *Monte Carlo Calculations in Nuclear Medicine: Applications in Diagnostic Imaging*. Institute of Physics Publishing. Chap. Anthropomorphic Phantoms, pp. 25–36.

Zaidi, H., & Tsui, B. M. W. (2009). Review of computational anthropomorphic anatomical and physiological models. *Proceedings of the IEEE*, Vol. 97, No. 12, pp. (1938–1953).

Zaidi, H., & Xu, X. G. (2007). Computational anthropomorphic models of the human anatomy: The path to realistic Monte Carlo modeling in radiological sciences. *Annual Review of Biomedical Engineering*, Vol. 9, pp. (471–500).

Zhu, Zhiyu, Tsui, B. M.W., & Segars, W. P. (2002). A simulation study of the effect of gating scheme on respiratory motion blurring in FDG lung PET. *IEEE Nuclear Science Symposium Conference Record*, pp. (1554–1558).